Soft Matter

PAPER

View Article Online
View Journal

Cite this: DOI: 10.1039/c7sm02378b

Competing failure modes in finite adhesive pads†

Tal Cohen,‡[abc] Chon U Chan ‡[a] and L. Mahadevan *[ade]

Received 3rd December 2017,
Accepted 15th January 2018

DOI: 10.1039/c7sm02378b

rsc.li/soft-matter-journal

Thin adhesive pads used to attach objects to each other often fail catastrophically. Here we consider the nature of failure of such a pad under loading parallel to the adhesive substrate. To determine the modes of failure of the pad and to understand what limits its load bearing capacity, we conduct experiments with finite pads composed of a soft adhesive layer with a stiff backing and load them parallel to the surface of adhesion. We find that two different peeling mechanisms emerge as a function of the slenderness of the adhesive pad: an interfacial peeling mechanism that starts close to the pulling end for very long pads, and an unstable curling mechanism that starts at the opposite end for relatively short pads. A minimal theoretical framework allows us to explain our observations and reveals the adhesive bond stiffness as a dominant parameter in defining the peeling mode. A phase diagram that delineates the different regimes of peeling modes brings our experiments and theory together. Our results suggest that unstable peeling by curling may be more common than previously thought, and could perhaps occur naturally in such examples as the gecko foot.

1 Introduction

Failure of the common adhesive pad – a layer of soft adhesive on a stiff backing – is a recurring nuisance that we have all had direct experience with. Although much ingenuity has been devoted to optimize their design for reuse in such instances as the Post-it note,§ in all artificial settings there is an inevitable compromise pitting reversible use and load bearing capacity. However, that compromise does not seem to transcend into the natural world. In the animal kingdom several species of insects and lizards have developed load-bearing capabilities using dry adhesive pads that perform reversibly at high switching rates.[1–3] To mimic this, numerous studies have attempted to identify and explain the role of hierarchical features in natural adhesives in such examples as gecko feet.[4–10] The small scale hierarchical features observed on natural dry adhesives have been explained to affect the strength of the adhesive bond by providing increased conformability to the substrate[11–13] as well as directionality[14–17] and the reversibility[18–21] of the attachment.

Here, we complement these studies by considering an additional effect, bond stiffness, which we show plays a significant role in the macro-scale peeling response of finite adhesive pads. Our work is inspired by a series of studies that suggest that the load bearing capacity of adhesive pads is a function of their longitudinal compliance.[22–25] This notion was further substantiated by the development of bio-inspired adhesive pads that can perform reversibly on multiple surfaces and with load bearing capacities scalable to those of natural systems.[22] In these studies, the adhesive layer was stiffened longitudinally by the attachment of a stiff backing to the soft adhesive layer, but to date only scaling arguments have been provided to explain why the load bearing capacity of the bi-layer composite is higher than that of a mono-layer with equivalent longitudinal stiffness.¶ Earlier studies on the failure of laminate composites[26,27] investigated the steady propagation of a crack-like peeling front,[28,29] and consider infinitely long adhesive layers being pulled off the substrate at a prescribed angle. More recent investigations considered initiation of peeling[30,31] and have shown that fingering patters form at the peeling front, as a flexible plate is lifted off an elastic film. These patterns are associated with the appearance of interfacial cavities that act as precursors to the propagation of the peeling front, thus resembling the

[a] Paulson School of Engineering and Applied Sciences, Harvard University, Cambridge, MA 02138, USA
[b] Department of Mechanical Engineering, Massachusetts Institute of Technology, Cambridge, MA 02138, USA
[c] Department of Civil & Environmental Engineering, Massachusetts Institute of Technology, Cambridge, MA 02138, USA
[d] Departments of Organismic and Evolutionary Biology, and Physics, Harvard University, Cambridge, Massachusetts, 02138, USA. E-mail: lmahadev@g.harvard.edu
[e] Kavli Institute for Nanobio Science and Technology, Harvard University, Cambridge, Massachusetts, 02138, USA

† Electronic supplementary information (ESI) available. See DOI: 10.1039/c7sm02378b

‡ These authors contributed equally to this work.

§ The Post-it note has multiple parcels of encapsulated glue, a few of which burst on every application, allowing the note to be reused.

¶ Available theories do not account for the finite length of the composite layer or the different dimensions and properties of the adhesive layer and the stiff backing, and consider a crack-like peeling front that propagate from the pulling end.

mechanism of fracture initiation in ductile metals.[32,33] Since the load bearing capacity of an adhesive layer is maximal when the peeling angle vanishes,[26,34] to determine the ultimate failure mechanism we focus on finite adhesive layers that are loaded parallel to the direction of the substrate. This allows us to account for both the dimensions of the composite adhesive layers that are composed of a soft adhesive with a stiff backing, and the stiffness of the adhesive bond at the interface.

In Section 2 we begin by describing the problem setting and our experimental observations of the different modes of peeling that are highly dependent upon the layer dimensions. In Section 3 we present a theoretical model that captures and explains those modes, and we study their sensitivity to design parameters of the composite layer. Based on a set of four dimensionless model parameters that naturally emerge from the formulation, we explore the deformation patterns and identify three distinct peeling modes. We find that debonding can be triggered either near the pulling end as an interfacial cavity, at the opposite end generating a peeling front that propagates towards the pulling end while visibly exhibiting curling of the free end, or by a combination of both. Our results yield a phase diagram which shows that the transition between different modes occurs for layers of realistic aspect ratios (length/thickness) and is highly dependent on the bond stiffness. In Section 4 we show that the transition between the peeling modes can be quantitatively captured *via* experiments and compares well with the analytical predictions. We conclude in Section 5 with a discussion of the possible manipulation of the unstable peeling mode to enable rapid adhesion-based locomotion, as well as the possible design of adhesives that can arrest cavitation while promoting a sequence of curling instabilities.

2 Observations

Our composite adhesive pads of length l are composed of two elastomeric layers of thickness t and t_b and Young's modulus E and E_b, as illustrated in Fig. 1(a) (preparation and characterization protocols of the elastomer are detailed in Appendix A). To observe the peeling mechanism, we attach the layer to a smooth glass plate and apply a horizontal displacement (Δz) to the edge of the adhered layer that is increased at a constant rate of 5–10 [mm min^{-1}] using a universal material tester (Instron 5566), as elaborated in Section 4. The experiment is synchronized with a high-speed camera (Phantom v9.1) to record the load-extension curve as well as the side and bottom views of the elastomer in contact with the glass. Fig. 1(b)–(d) show snapshots taken from the high-speed movies of three representative layers of different lengths in their initial state (first image on the left), and during peeling (second and third images), where darker regions show lost contact with the glass substrate.

Examining the peeling behavior for the shortest pads (Fig. 1(b)) we notice that the peeling front propagates from

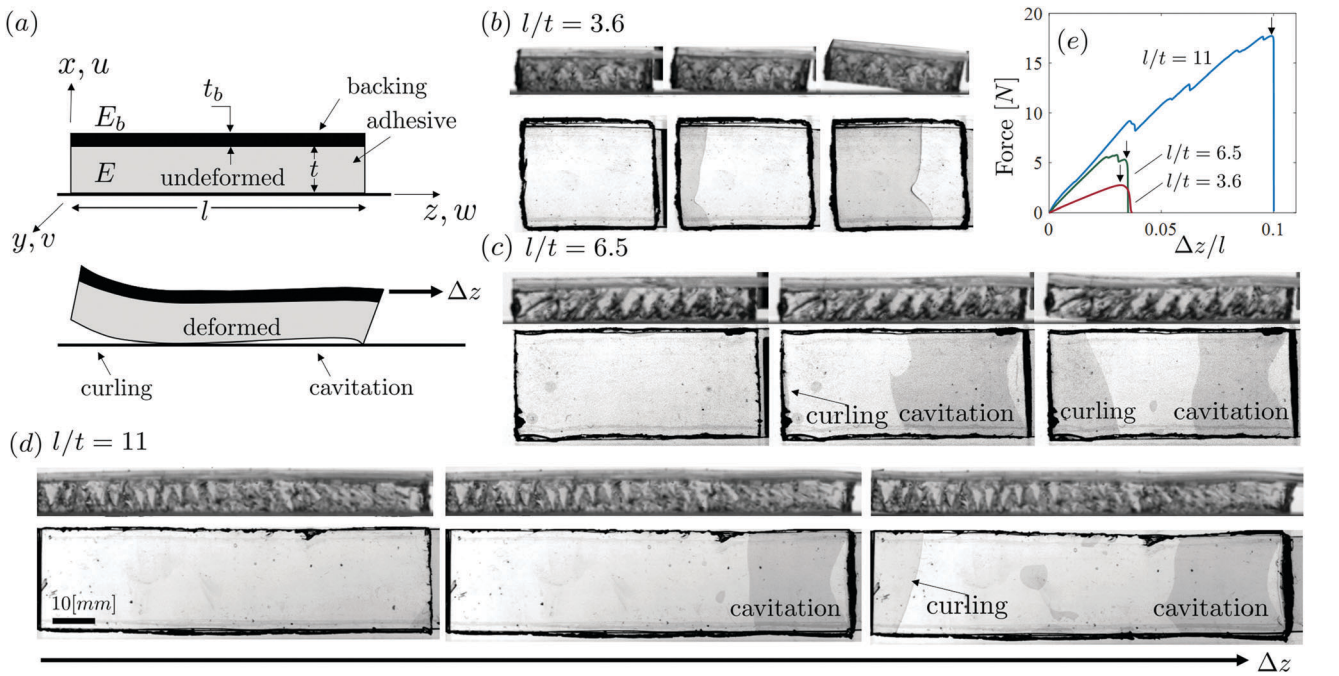

Fig. 1 Problem setting and experimental observations. (a) Illustration of the layer including dimensions, material parameters and the coordinate system (x,y,z). A schematic of the deformed configuration induced by a displacement Δz applied at the leading edge along the longitudinal direction. In this case both cavitation and curling appear. (b–d) Snapshots of high-speed movies (Movies S1–S3, ESI†) capturing the peeling events with increasing applied displacement (Δz) from left to right. The first image on the left shows the undeformed state. Samples of the pad with three different aspect ratios are shown, with $l/t \cong 3.6$, 6.5, 11 respectively. For all samples the elastic moduli and thickness of the adhesive layer and the backing are E = 0.17 [MPa], t = 8.3 [mm] and E_b = 2 [MPa], t_b = 2.4 [mm], respectively. Side views of the layers are shown on the top. The bottom view of the layer through the glass substrate is also shown below – the darker regions correspond to areas that have detached from the substrate. (e) Load-extension curves corresponding to the three peeling tests. The arrows indicate onset of curling.

the end that is opposite from the pulling end. We refer to this mode of peeling as the curling mode, since it involves curling of the far end of the layer as it lifts off of the surface. For intermediate length pads, as seen in Fig. 1(c) curling is accompanied by a debonding event that is initiated as an interfacial cavity near the pulling end. Finally for very long adhesive pads, as shown in Fig. 1(d), the interfacial cavity grows to a nearly constant length until curling is triggered suddenly just before the onset of failure. For long adhesive pads, this cavity appears much earlier and is followed by dynamic shedding events wherein smaller cavities detach from the main cavity and subsequently disappear (see ESI† for movies).

In Fig. 1(e), we complement our qualitative observations of peeling by measuring the force–displacement curves that correspond to the three peeling tests in Fig. 1(b)–(d). We find that in all cases curling (indicated by an arrow) is followed by a significant reduction in the load until complete detachment and failure. Although the force displacement curve for the shortest layer is smooth, for the larger aspect ratio specimens, cavitation events result in a slight drop in load (see ESI† for movies). Thus, in a force-controlled loading scenario we expect to see dynamic instabilities, although in all cases, the ultimate failure mode occurs *via* curling. We note that nonuniform deformations that resemble fingering instabilities in the transverse direction are sometimes observed,[35–37] but we will not focus on these here.

Overall, these observations suggest that the mode of peeling is highly dependent upon the dimensions of the layer and that the different peeling mechanisms can appear simultaneously. Nevertheless, what ultimately limits the load bearing capacity of the layer is determined by the onset of curling at the far end. Therefore, we turn to understanding this peeling mechanism and its sensitivity to the geometry and stiffness of the composite layer.

3 Theory

Although many studies of peeling generally assume a rigid adhesive bond up to loss of contact, in soft systems with weak bonding, bond deformations are non-negligible and the bond stiffness can significantly influence the peeling response as it allows for the redistribution of stresses within the layer prior to detachment. To evaluate the regime in which the bond stiffness becomes non-negligible, we consider a scenario where a normal stress σ is applied on the top face of a segment of the soft adhesive layer (without the backing, for simplicity). If the bond is rigid, this will generate a displacement $u = \sigma t/E$. Otherwise, an additional displacement will arise due to bond deformation and $u = \sigma t/E + \sigma/k$ where k represents the bond stiffness per unit area.‖ Bond stiffness can be neglected if $kt/E \gg 1$. However, for soft interfaces, the bond stiffness (k) is dictated by the density of bonds per unit area, and dependent on the features of the interface and on the method of attachment, and it can even vary over time.[38,39] Accounting for a finite bond stiffness captures the local increase in compliance that can be induced, for example, by hierarchical features of the bonding interface or by the distribution of molecular bonds. Hence, to capture the critical state at which debonding is triggered as a response to horizontal displacement (Δz), we model the attachment of the adhesive pad to the substrate *via* a homogeneous distribution of springs at the interface with a maximum allowable displacement from the substrate. We note that the bond stiffness considered herein is not merely an alternative representation of the more commonly used adhesion energy, since it does not represent the critical debonding state. Considering adhesives for which small-strains are sufficient to generate detachment, a linearly elastic material response can be assumed and the deformation pattern at the onset of debonding is independent of the magnitude of the applied displacement. According to this framework, debonding will occur where the normal displacement from the substrate is maximal.

There are a few dimensionless model parameters that characterize our system given by

$$\alpha = \frac{t_b}{t}, \quad \beta = \frac{E_b t_b}{Et}, \quad \gamma = \frac{kt}{E} \tag{1}$$

which, together with the aspect ratio l/t of the pad, fully define the problem. Here α is the thickness ratio of the backing to the adhesive layer, β represents the ratio of longitudinal stiffnesses,** and γ is a dimensionless measure of the bond stiffness. We note the difference between the dimensionless bond stiffness γ, and the elasto-capillary number $n = \tau/(Et)$, where τ represents the surface tension.[40] The later is associated with the in-plane properties of the interface, and the former with the out of-plane response.

3.1 Mathematical formulation

We consider an elastic adhesive that, in its undeformed state, occupies the region $0 \le x \le t$, $-\infty < y < \infty$, and $0 \le z \le l$, as shown on Fig. 1(a). One face of the adhesive, at $x = 0$, is attached to a rigid substrate, while the other, at $x = t$, is perfectly bonded to an elastic backing of thickness (t_b). To peel the adhesive, we apply a displacement (Δz) by pulling the backing along the longitudinal axis at $z = l$. Assuming plane-strain conditions, this results in the displacement fields

$$u = u(x,z), \quad v = 0, \quad w = w(x,z) \tag{2}$$

along the (x,y,z) directions, respectively (Fig. 1(a)). The non-zero strain components are thus

$$\varepsilon_x = \frac{\partial u}{\partial x}, \quad \varepsilon_z = \frac{\partial w}{\partial z}, \quad \varepsilon_{xz} = \frac{1}{2}\left(\frac{\partial u}{\partial z} + \frac{\partial w}{\partial x}\right) \tag{3}$$

Kinematic constraints. We make two assumptions on the deformation field. First, we assume the adhesive layer to be incompressible, so that

$$\frac{\partial u}{\partial x} + \frac{\partial w}{\partial z} = 0, \quad (\varepsilon_x + \varepsilon_z = 0) \tag{4}$$

‖ Note the difference between the 'bond stiffness' (k) which refers to the stiffness (per unit area) of the adhesive bond at the interface, and the 'adhesive modulus' (E) which refers to the elastic modulus of the adhesive layer.

** Notice also that $\alpha^2\beta$ represents the ratio of bending stiffnesses between the two layers.

Secondly, we assume that, in the adhesive layer, planes that are initially normal to the longitudinal axis remain planar upon deformation. Both these assumptions may be justified for the case of thin elastomers. The longitudinal deformation (2)[3] can now be specialized to

$$w = w_0(z)\left(1 - \frac{x}{t}\right) + w_t(z)\frac{x}{t} \tag{5}$$

where $w_0(z) = w(0,z)$ and $w_t(z) = w(t,z)$ represents the displacement of the top and bottom surfaces of the adhesive layer, respectively. Combining the above kinematic constraints (4) and (5), and integrating the result yields a relation for the normal displacement (2)[1] of the form

$$u = u_0(z) - \frac{x}{2}\left(w_0'(z)\left(2 - \frac{x}{t}\right) + w_t'(z)\frac{x}{t}\right) \tag{6}$$

where $u_0(z) = u(0,z)$, and the superposed prime denotes differentiation along the longitudinal coordinate $(\cdot)' = \mathrm{d}(\cdot)/\mathrm{d}(z)$.

The deformation field is now fully defined by a set of three functions (u_0,w_0,w_t) that vary along the longitudinal coordinate (z). For further reference, we can write the normal displacement of the top surface $u_t = u(t,z)$ as

$$u_t = u_0 - \frac{t}{2}(w_0' + w_t') \tag{7}$$

and the strain components (3) now read

$$\begin{aligned} \varepsilon_x &= -\varepsilon_z = (w_0' - w_t')\frac{x}{t} - w_0' \\ \varepsilon_{xz} &= \frac{1}{2}\left(u_0' - (w_0 - w_t)\frac{1}{t} - w_0''x + (w_0'' - w_t'')\frac{x^2}{2t}\right) \end{aligned} \tag{8}$$

Elastic energy. We now proceed to write the elastic energy absorbed by the composite layer for a given deformation. The longitudinal strain energy density is composed of three contributions; $\mathscr{E}_A$ – the energy of the adhesive layer, $\mathscr{E}_B$ – the energy of the backing, and $\mathscr{E}_C$ – the energy associated with the compliance of the adhesive bonds. For the adhesive layer, given the plane-strain conditions, the longitudinal strain energy density in the adhesive layer is

$$\mathscr{E}_A = \frac{2}{3}E\int_0^t \left(\varepsilon_x{}^2 + \varepsilon_{xz}{}^2\right)\mathrm{d}x \tag{9}$$

where E is the elastic modulus. Inserting the strain components (8) into the above expression then yields

$$\begin{aligned} \mathscr{E}_A = \frac{E}{18t}\Big[&\left(8w_0''^2 + 9w_0''w_t'' + 3w_t''^2\right)\frac{t^4}{20} - u_0''(2w_0'' + w_t'')t^3 \\ &+ (w_0 - w_t)(2w_0'' + w_t'')t^2 \\ &+ \left(3u_0'^2 + 4w_0'^2 + 4w_0'w_t' + 4w_t'^2\right)t^2 \\ &- 6u_0'(w_0 - w_t)t + 3(w_0 - w_t)^2\Big] \end{aligned} \tag{10}$$

Now, we turn to consider the elastic energy in the backing which we assume to be sufficiently thin such that it can be modeled as an isotropic incompressible elastic plate that stores energy in tension and bending, allowing us to write

$$\mathscr{E}_B = \frac{2E_b t_b}{3}w_t'^2 + \frac{E_b t_b^3}{18}u_t''^2 \tag{11}$$

The last remaining contribution to the elastic potential is that of the adhesive bond which depends on the bond stiffness k and on the displacements at the adhesive interface (u_0,w_0). Defining k as the stiffness of the interface, we write the energy stored at the adhesive interface as

$$\mathscr{E}_C = \frac{1}{2}k\left(u_0{}^2 + w_0{}^2\right) \tag{12}$$

With the three contributions given in (10)–(12), the elastic energy density, $\mathscr{E} = \mathscr{E}_A + \mathscr{E}_B + \mathscr{E}_C$, can be written in terms of three independent functions (u_0,w_0,w_t), or equivalently in terms of the dimensionless generalized set $\mathbf{q} = (q_1,q_2,q_3)$, and its derivatives up to the third order. One possible set, that we use here for analytical compactness is

$$\begin{aligned} q_1(\zeta) &= w_t(t\zeta)/t \\ q_2(\zeta) &= (w_0(t\zeta) + w_t(t\zeta))/t \\ q_3(\zeta) &= u_t(t\zeta)/t \end{aligned} \tag{13}$$

that are functions of the dimensionless longitudinal coordinate

$$\zeta = \frac{z}{t} \tag{14}$$

The total elastic energy (per unit width in the out of plane direction) is then given by

$$\Phi = \int_0^l (\mathscr{E}_A + \mathscr{E}_B + \mathscr{E}_C)\mathrm{d}z \tag{15}$$

and may be written in general form as

$$\Phi = \int_0^{l/t} \mathscr{E}\left(\mathbf{q}, \mathbf{q}^{(1)}, \mathbf{q}^{(2)}, \mathbf{q}^{(3)}\right)t\mathrm{d}\zeta \tag{16}$$

For completeness we write the strain energy density contributions $\mathscr{E}_A$, $\mathscr{E}_B$ and $\mathscr{E}_C$, in terms of $\mathbf{q}$ and its derivatives (represented by the superscript (i)), in eqn (B1)–(B3) of Appendix B. Extremizing the energy yields a governing system of three fourth-order linear ordinary differential equations that depend on a single independent field variable (ζ)

$$\begin{aligned} 4q_1^{(4)} + 3q_2^{(4)} + 20q_3^{(3)} - 80(1 + 6\beta)q_1^{(2)} + 100q_2^{(2)} + 240q_3^{(1)} \\ + 120(4 + 3\gamma)q_1 - 120(2 + 3\gamma)q_2 = 0 \end{aligned} \tag{17}$$

$$\begin{aligned} 3q_1^{(4)} + 6q_2^{(4)} + 20q_3^{(3)} + 100q_1^{(2)} - 10(20 + 9\gamma)q_2^{(2)} - 60(2 + 3\gamma)q_3^{(1)} \\ - 120(2 + 3\gamma)q_1 + 120(1 + 3\gamma)q_2 = 0 \end{aligned} \tag{18}$$

$$2\alpha^2\beta q_3^{(4)} - q_1^{(3)} - q_2^{(3)} - 6q_3^{(2)} - 12q_1^{(1)} + 3(2 + 3\gamma)q_2^{(1)} + 18\gamma q_3 = 0 \tag{19}$$

As observed, the three dimensionless model parameters defined in (1) emerge naturally within the formulation. This is a 12th order system that requires 12 boundary conditions.

Boundary conditions. Since the bonding to the rigid substrate involves displacements of the bottom surface $(x = 0)$ that

are penalized by accumulation of elastic energy in the adhesive bonds, the only boundary constraint imposed on the layer is the displacement at the pulling end, namely

$$(u(t,l),w(t,l)) = (0,\Delta z) \tag{20}$$

which can be translated to dimensionless terms as

$$q_1(l/t) = \Delta z/t, \quad q_3(l/t) = 0 \tag{21}$$

Additionally the natural boundary conditions that emerge from the Euler–Lagrange derivation are

$$4q_1^{(3)} + 3q_2^{(3)} + 20q_3^{(2)} - 120(1+4\beta)q_1^{(1)} + 60q_2^{(1)} = 0 \tag{22}$$

$$3q_1^{(3)} + 6q_2^{(3)} + 20q_3^{(2)} + 120q_1^{(1)} - 90(2+\gamma)q_2^{(1)} - 180\gamma q_3 = 0 \tag{23}$$

$$2\alpha^2\beta q_3^{(3)} - q_1^{(2)} - q_2^{(2)} - 6q_3^{(1)} - 12q_1 + 6q_2 = 0 \tag{24}$$

$$4q_1^{(2)} + 3q_2^{(2)} + 20q_3^{(1)} + 40q_1 - 20q_2 = 0 \tag{25}$$

$$3q_1^{(2)} + 6q_2^{(2)} + 20q_3^{(1)} + 40q_1 - 20q_2 = 0 \tag{26}$$

$$\alpha^2\beta q_3^{(2)} = 0 \tag{27}$$

To solve the system for a finite layer we must employ boundary conditions at both ends, *i.e.* $\zeta = 0$ and at $\zeta = l/t$. At $\zeta = 0$ we adopt the natural boundary conditions (22)–(27) and at $\zeta = l/t$ we employ the two conditions in (21) with (24)–(27).

It is useful to look at a couple of different limits of the above equations:

Vanishing adhesive stiffness. If the longitudinal stiffness of the adhesive layer is significantly smaller than that of the backing then $\beta \gg 1$ and (assuming finite values of $\alpha^2\beta$ and γ) eqn (22) reads $q_1^{(2)} = 0$ and thus the longitudinal displacement of the top layer ($w_t = q_1 t$) must be a linear function. Then, employing boundary condition (22), which reads $q_1^{(1)} = 0$, implies that the longitudinal displacement of the backing is constant $q_1 \equiv \Delta z/t$. This result intuitively suggests a simple shear scenario, in which no normal displacement occurs ($q_2 = q_3 = 0$). However, for finite bond stiffness, the moment induced by the pulling force can only be equilibrated by an asymmetric deformation field. It will be shown in the next section that this asymmetric response leads to curling.

Infinite bond stiffness. If the bonding between the adhesive layer and the substrate is rigid ($\gamma \to \infty$), then no displacement occurs at $x = 0$ and $u_0 = w_0 \equiv 0$. In terms of the dimensionless variables this implies that $q_1 = q_2 = q$ and $q_3 = -q'/2 = p$. Applying these constraints in the Euler–Lagrange formulation is equivalent to adding the first two eqn (17) and (18), to the derivative of the third eqn (19), and after some algebra yields the single equation 6th order equation

$$5\alpha^2\beta p^{(6)} - 3p^{(4)} + 20(5+12\beta)p^{(2)} - 60p = 0 \tag{28}$$

Although the rigid bonding constraint leads to a reduced form of the governing eqn (17)–(19), the absence of interface compliance restricts the distribution of stress within the layer and leads to localization of the deformation near the pulling end (this will be shown from the integration results in the next section). Hence, this form can only be applied to study failure mechanisms that initiate near the pulling end, thus emphasizing the need for the higher order description.

Vanishing backing thickness. The thickness of an isotropic backing material influences both its extensibility and bending stiffness. Nonetheless, for $\alpha \ll 1$ and finite β, the first term in (19) can be neglected, reducing the order of the system. However, this does not significantly reduce the complexity of its solution nor the results.

3.2 Results

For a finite layer, if the model parameters ($\alpha,\beta,\gamma,l/t$) are finite, no further simplification of the analytical representation is possible and boundary conditions must be applied at both ends of the layer. The roots of the characteristic equation associated with the governing system of eqn (17)–(19) are obtained numerically, and the solution obtained by employing six boundary conditions at each end of the finite layer, as explained in the previous section.

In Fig. 2a, we show representative results for the normal displacement of the bottom surface ($u_0/\Delta z$) for layers of varying aspect ratios, with $\alpha = 0.1$, $\beta = 1.5$ and $\gamma = 0.03$, debonding will initiate where the normal displacement is maximal. It is observed that for sufficiently long and thin layers ($l/t = 30$), the deformation is concentrated near the pulling end ($z = l$), where the maximum lift off of the substrate appears in the form of an interfacial cavity. In this situation, since the deformation is localized, debonding at the cavity will spread the deformation to effect a larger region. However it will not necessarily lead to failure, implying that a new stable configuration is plausible. From here on, we refer to peeling that initiates by formation of a cavity as cavitation dominated, which in Fig. 2a is observed for aspect ratios in the range $l/t \geq 19$. The nucleation of interfacial cavities as a precursor to the formation of a peeling front has been previously indicated for infinitely long layers and shown to appear at a load much higher than that required to propagate it.[30,41] This behavior is also observed in Fig. 1(e), where cavitation events result in only a slight drop in load whereas, in all cases, failure ultimately occurs by curling which is followed by a significant reduction of load.

As l/t becomes smaller, an additional region of localization emerges at the other end of the layer ($z = 0$) and becomes dominant as the maximum lift off is equal at both fronts ($l/t \sim 19$), as shown in Fig. 2(a). In this state, debonding may be triggered simultaneously at both ends, and for even smaller aspect ratios it will be triggered at the far end ($z = 0$). This leads to a redistribution of stresses on a smaller adhesion area, and in turn intensifies the stresses at the interface that will lead to further debonding. Then, rather than having a peeling front that propagates backward from the pulling end, a curling mode in which the peeling front propagates forward from the opposite end is seen. This curling dominated regime is thus defined for situations in which both curling and cavitation are apparent but with peeling initiation at the free end ($z = 0$), and is seen when $8 \leq l/t \leq 19$. Finally, for even smaller aspect ratios ($l/t \leq 8$), the cavitation maximum near the leading edge is no longer apparent and thus we refer to this regime as the curling only regime. We note that as the aspect ratio further decreases below $l/t \sim 3$ the curvature of the backing

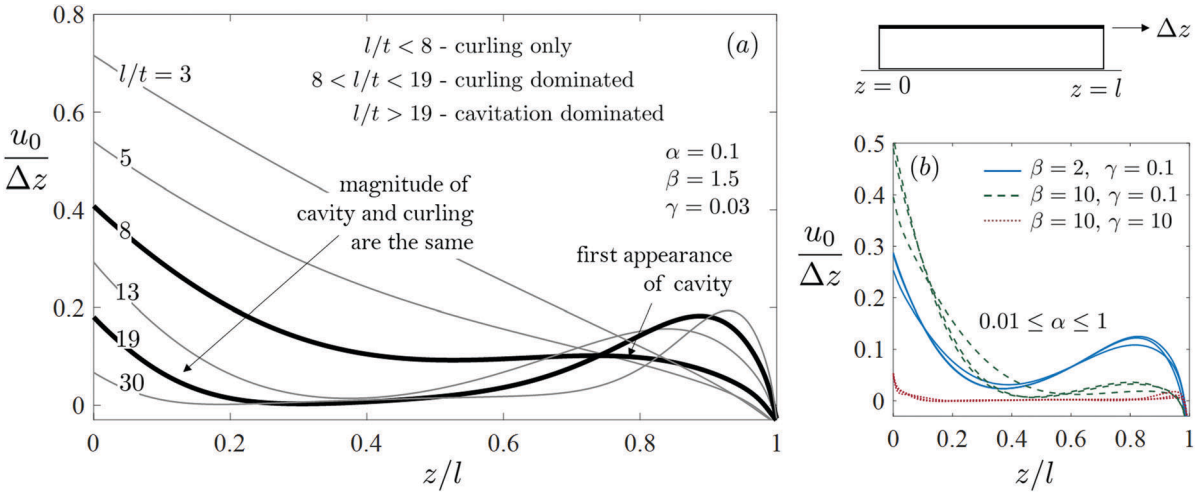

Fig. 2 Normal displacement of the bottom surface ($u_0/\Delta z$) for layers of different properties and dimensions. (a) Sensitivity to aspect ratio: patterns are shown for layers with aspect ratios in the range $3 \le l/t \le 30$, and with $\alpha = 0.1$, $\beta = 1.5$, and $\gamma = 0.03$. Three distinct regimes of response are observed and the transition between them indicated by thick black curves. (b) Sensitivity to model parameters: patterns are shown for $\alpha = 0.01, 0.1, 1$. Different colored curves distinguish between three sets of parameters with two different values of $\beta = 2, 10$ and two different values of $\gamma = 0.1, 10$, while all curves are calculated with $l/t = 10$.

decreases and the layer detaches by a mode that is akin to rigid body rotation.

To investigate the effect of the system properties on the different modes of failure, we follow the dependence of the solution on the system parameters. In Fig. 2(b), we examine the variation of the deformation response on α, and do not see much sensitivity for values in the range $0.01 \le \alpha \le 1$ (thus implying insensitivity also to scaled bending stiffness ratios that are shown in the range $2 \times 10^{-4} \le \alpha^2\beta \le 10$). However, varying the scaled longitudinal compliance β does change the response curves significantly, in agreement with the scaling argument given in ref. 22; as β increases for the same values of γ, there is a transition to curling-dominated failure (blue and green curves). Finally, varying the scaled bond stiffness γ, we see that there is a significant effect due to this parameter as well; as γ increases for the same value of β, there is a transition to cavitation-dominated failure associated with more strongly localized deformations (as shown by the green and red curves in Fig. 2(b)).

To obtain a better understanding on the effect of model parameters in dictating the peeling mode, and considering the insensitivity to α, we use the dimensionless parameters (β,γ,l/t) as a basis to examine the sensitivity and construct phase diagrams in Fig. 3, from which it becomes apparent that the curling mode dominants as β increases. Additionally, in it is observed that reducing the scaled bond stiffness γ further increases the range in which curling is dominant. Overall, peeling by cavitation is dominant only for large aspect ratio specimens that either have small stiffness ratios (β) or high bonding stiffness (γ). As the layer becomes longer, the deformation localizes at its ends and available theories that consider infinitely long layers become valid. Most importantly, our results show that the scaled bond stiffness (γ) significantly influences the peeling mode, so that the theories that assume infinite bond stiffness ($\gamma \to \infty$) are limited to high aspect-ratio specimens.

In view of Fig. 3 we can consider two limiting cases in which classical theories breakdown. First, theories that consider

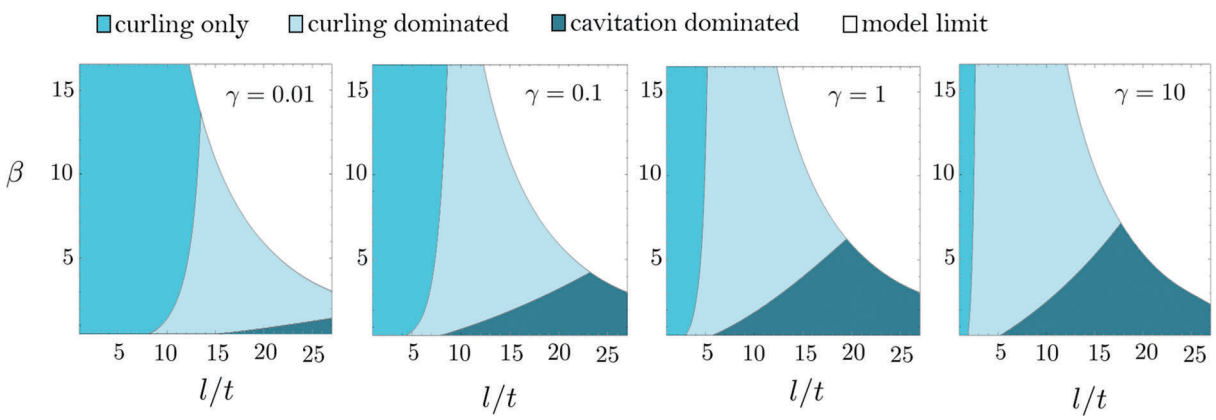

Fig. 3 Phase diagrams in the scaled stiffness β aspect ratio l/t plane, shown for four different scaled bond stiffness γ values and calculated with scaled thickness $\alpha = 0.2$. The three peeling modes that are illustrated for a specific set of model parameters in Fig. 2, are distinguished by the different shades of blue.

inextensible layers ($\beta \to \infty$) predict infinite load bearing capacity.[26,42] In contrast, our quantitative identification of an additional peeling mechanism that is dominant in this limit provides a realistic explanation of the observed response. Intuitively, when the backing is inextensible and pulled along the direction of the substrate, the deformation is no longer localized near the pulling edge (as assumed in classical theories) and curling of the far end will ultimately lead to failure. Secondly, in the limit when the adhesive bond is compliant, *i.e.* $\gamma \ll 1$, the deformation of the adhesive layer cannot localize and interfacial cavitation is suppressed, in contrast with classical theories which operate in the limit $\gamma \gg 1$.

4 Experiments

To test our theoretical predictions using quantitative experiments that complement our initial observations, we conducted a systematic experimental investigation to examine the sensitivity of the peeling response to specimen dimensions and material properties. Given the insignificant influence of α†† predicted by the theoretical analysis, we consider the sensitivity to β, γ and l/t. Since the curling only mode is clearly indicated in the experiments by a smooth force displacement curve and absence of cavities (see Fig. 1(e)), we focus on the transition from a curling only response to a curling dominated response, in which both cavitation and curling are active.

Although varying the layer dimensions and elastic moduli is relatively straightforward (see Appendix A for further details on material preparation), controlling (and measuring) the bond stiffness per unit area (k) can be more challenging. On the other hand, to study the influence of the bond stiffness on the peeling response we vary its dimensionless counterpart $\gamma = kt/E$. Thus, by holding k constant and varying E/t we can experimentally control γ. To assure minimal variation in k values we employ a simple experimental protocol in which the layers are attached to the substrate by applying $\sim$ 8 [kPa] of normal pressure to ensure proper bonding for similar lengths of time before the experiments are carried out. Additionally, we verify that the force displacement curve is insensitive to changes in applied normal pressure in the range 2.6–26 [kPa].

We map out the phase boundary experimentally by conducting a series of experiments with samples made of identical materials while gradually reducing the aspect ratio (l/t), as shown in Fig. 4. We mark cavitation events by a triangle, and curling modes using a star. Experiments were carried out using six sets of samples (Table 1) that can be divided into two groups; group 1 is indicated in blue and group 2 in red, and are distinguished by an order of magnitude difference in t/E, and thus an order of magnitude difference in γ. To verify repeatability of our results, tests were performed on three independent samples for each set of parameter values. Theoretical predictions of the phase boundary for varying γ values are also shown for comparison *via* black curves. We note that there is a good qualitative agreement between the theoretical and experimental phase boundary curves. Given the observed and calculated dependence of the transition between the modes of failure, we estimate the bond stiffness to be $k \sim 4$ [N mm^{-3}]. Assuming the average stiffness of a single van der Waals interaction is $\sim$ 1 [N m^{-1}], our observed k corresponds to an areal bond density of $\sim 4 \times 10^3$ [mm^{-2}]. This yields an indirect measurement of a typical bond–bond distance $\sim$30 μm, which would otherwise be difficult to measure.

†† The variation of the thickness ratio α in our samples is up to 35%.

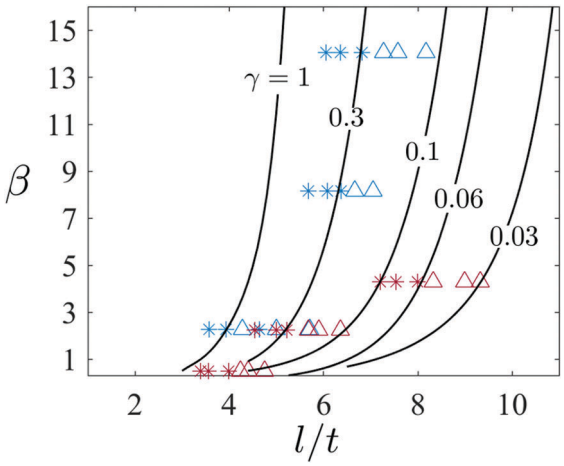

Fig. 4 Phase boundary curves for transition between curling only and curling dominant modes. Experimental results are indicated by triangles and stars. Blue markers are for 'group 1' layers, and red markers for 'group 2' layers, as indicated in Table 1. Stars correspond to samples that exhibited a curling-only response. Triangles correspond to samples in which peeling involved cavitation. For comparison, analytical curves for varying γ values (with α = 0.2) are shown in black.

Table 1 Dimensionless model parameters (α,β,γ) for six sets of samples, divided into two groups. Since the bond stiffness per unit area k is unknown, the dimensionless value $\gamma = (t/E)k$ is written with k [MPa mm^{-1}] as a coefficient of the measured value – t/E [mm MPa^{-1}]. The ratio in γ values of 'group 1' and 'group 2' is $\sim$10

	Group 1			Group 2		
α	0.29	0.39	0.29	0.4	0.36	0.27
β	14	8.1	2.3	4.2	2.2	0.49
γ	78k	86k	89k	8.0k	11k	8.6k

5 Conclusions

Our study has considered the failure modes of finite dry adhesive bilayers as they peel away from a substrate when loaded along the direction of the adhesive interface. Although theories on peeling regularly consider the propagation of a steady peeling front following interfacial cavitation near the pulling end towards the opposite end, our combined analytic and experimental investigation reveals a second (unstable) failure mode for finite adhesive layers that is associated with curling at the far end, and propagates towards the pulling end. While curling triggers unstable peeling, interfacial cavities do not necessarily lead to failure. A systematic investigation of the influence of the model parameters and layer dimensions on the

peeling response shows that the peeling mode is highly sensitive to the relative compliances of the adhesive and the backing. Moreover, although available theories regularly assume the adhesive bond to be rigid up to loss of contact, our introduction of the bond stiffness emerges as a key parameter in determining the peeling mode, thus providing an additional explanation of the role of hierarchical features observed in natural dry adhesives. Although our theoretical model can capture the different peeling modes and provides reasoning for their stable/unstable nature, a more elaborate theoretical model is needed to quantify the stability threshold and should be subject for future work.

A phase diagram that shows the transition between (unstable) curling and (stable) cavitation peeling modes for varying model parameters can serve as a set of design rules for adhesive selection. Navigating through this design space might allow for the active switching between stable and unstable states, and can possibly facilitate rapid maneuverability of adhesion-based locomotion. For example, the rapid peeling capabilities observed in geckos that have been shown to switch between attached and detached states within 20 [ms] has been previously attributed to active muscular control of the observed curling in the direction normal to adhesive plane.[14] Our study suggests an alternative explanation: by loading the adhesive pad parallel to itself using tangentially acting muscles, the gecko foot could curl passively and thus rapidly switch from a stable adhered state to unstable peeling. Testing this hypothesis by studying EMG recordings while measuring force–extension curves is a natural next step, as is the influence of the rate of peeling on the observed phenomena.

Conflicts of interest

There are no conflicts to declare.

Appendix A – layer fabrication and surface preparation

Elastic modulus tuning

The elastomeric adhesive layer was fabricated by mixing Sylgard 184 (Dow Corning) with a softer elastomer, Sylgard 527 (Dow Corning). The two are first mixed individually with the standard monomer to crosslinker mixing ratios (*i.e.* 10 : 1 and 1 : 1 by weight), then they are mixed at various mass ratios. The elastic modulus of the resultant material is measured by a tensile force tester (Instron 5566) according to the ASTM international standard test method D638-14. The dependence of the elastic modulus on the mixing ratio is shown in Fig. 5, and allows us to fabricate adhesive layers with modulus between 41 to 680 [kPa]. The backing layer is made from Sylgard 184 (Dow Corning) silicone elastomer with modulus that can be tuned by deviating from the standard crosslinker mixing ratio (10 : 1 by weight). We find that the reproducibility of the mechanical properties is low when the mixing ratio deviates too much from the value recommended by the manufacturer, so that we use two mixing ratios 10 : 1 and 13 : 1, which leads to elastic moduli of 2.1 and 1.2 [MPa], respectively.

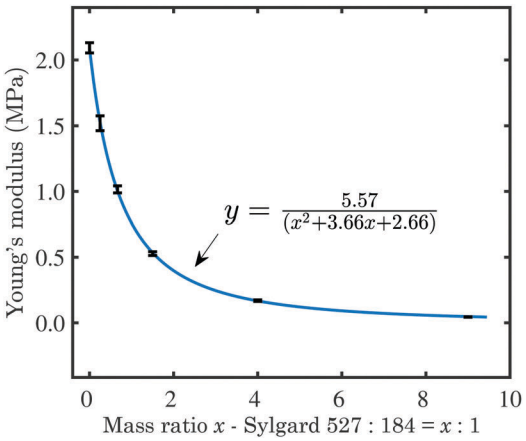

Fig. 5 Dependence of the elastic modulus on cross-linking mixing ratios.

Layer preparation

Silicone elastomers with the targeted mixing ratios are mixed and degassed with a centrifugal mixer (Thinky AR-100). They are then poured on polystyrene dishes to the targeted thickness, and allowed to set still before placing in a carefully leveled oven at 75° for at least 5 hours. Once the adhesive layer is cured, the backing layer is poured and cured on top with the same procedure. To separate two layers at the clamping tongue, a 65 μm thick plastic film is attached to the cured adhesive layer before pouring the backing layer mixture. The fully cured bilayer elastomer is then engraved by a laser cutter (VersaLaser 30 W) and diced with a razor blade to the desired dimensions. The width of the adhesive pads is either 25 or 30 [mm].

Substrate preparation

The substrates are glass plates cleaned in an ultrasonic bath (sequentially with acetone and isopropanol alcohol) and a plasma cleaner.

Appendix B – energy densities for the elastomer, backing and adhesive bonds

The longitudinal energy densities (10)–(12), written in terms of the dimensionless field variables (13) are

$$\begin{aligned}\mathscr{E}_{\mathrm{A}} = \frac{Et}{18}\Big(\frac{1}{20}\Big(&2(q_1'')^2+3q_1''q_2''+3(q_2'')^2\Big)+q_3'(q_1''+q_2'')\\&+(2q_1-q_2)(q_1''+q_2''+6q_3'')\\&+4\Big((q_1')^2-q_1'q_2'+(q_2')^2\Big)+3(q_3')^2\\&+3(2q_1-q_2)^2\Big)\end{aligned} \tag{B1}$$

$$\mathscr{E}_B = \frac{Et}{18}\left(\frac{12E_b t_b}{Et}(q_1')^2 + \frac{E_b t_b^3}{Et^3}(q_3'')^2\right) = \frac{Et}{18}\beta\left(12(q_1')^2 + \alpha^2(q_3'')^2\right) \quad \text{(B2)}$$

$$\mathscr{E}_C = \frac{kt^2}{8}\left((q_2' + 2q_3)^2 + 4(q_2 - q_1)^2\right) = \frac{Et}{8}\gamma\left((q_2' + 2q_3)^2 + 4(q_2 - q_1)^2\right) \quad \text{(B3)}$$

Acknowledgements

We thank the Harvard MRSEC DMR 1420570, NSF IOS 1257946, ARO W911NF-0166 and the MacArthur Foundation (L. M.), and A*STAR International Scholarship (C. UC.), for partial financial support.

References

1 D. Labonte and W. Federle, *Philos. Trans. R. Soc., B*, 2015, **370**, 20140027.
2 D. Labonte, C. J. Clemente, A. Dittrich, C.-Y. Kuo, A. J. Crosby, D. J. Irschick and W. Federle, *Proc. Natl. Acad. Sci. U. S. A.*, 2016, **113**, 1297–1302.
3 J. A. Williams, *J. Phys. D: Appl. Phys.*, 2014, **48**, 015401.
4 H. E. Jeong, J.-K. Lee, H. N. Kim, S. H. Moon and K. Y. Suh, *Proc. Natl. Acad. Sci. U. S. A.*, 2009, **106**, 5639–5644.
5 A. Y. Y. Ho, L. P. Yeo, Y. C. Lam and I. Rodrguez, *ACS Nano*, 2011, **5**, 1897–1906.
6 S. N. Gorb, M. Sinha, A. Peressadko, K. A. Daltorio and R. D. Quinn, *Bioinspiration Biomimetics*, 2007, **2**, S117.
7 A. Pattantyus-Abraham, J. Krahn and C. Menon, *Front. Bioeng. Biotechnol.*, 2013, **1**, 22.
8 K. Autumn, *MRS Bull.*, 2007, **32**, 473–478.
9 K. Autumn, M. Sitti, Y. A. Liang, A. M. Peattie, W. R. Hansen, S. Sponberg, T. W. Kenny, R. Fearing, J. N. Israelachvili and R. J. Full, *Proc. Natl. Acad. Sci. U. S. A.*, 2002, **99**, 12252–12256.
10 K. Autumn, A. Dittmore, D. Santos, M. Spenko and M. Cutkosky, *J. Exp. Biol.*, 2006, **209**, 3569–3579.
11 H. Gao, X. Wang, H. Yao, S. Gorb and E. Arzt, *Mech. Mater.*, 2005, **37**, 275–285.
12 C. Greiner, E. Arzt and A. Del Campo, *Adv. Mater.*, 2009, **21**, 479–482.
13 D. Labonte and W. Federle, *J. R. Soc., Interface*, 2016, **13**, 20160373.
14 Y. Tian, N. Pesika, H. Zeng, K. Rosenberg, B. Zhao, P. McGuiggan, K. Autumn and J. Israelachvili, *Proc. Natl. Acad. Sci. U. S. A.*, 2006, **103**, 19320–19325.
15 K. Autumn and A. M. Peattie, *Integr. Comp. Biol.*, 2002, **42**, 1081–1090.
16 S. Xia, L. Ponson, G. Ravichandran and K. Bhattacharya, *Phys. Rev. Lett.*, 2012, **108**, 196101.
17 S. Kim, M. Spenko, S. Trujillo, B. Heyneman, V. Mattoli and M. R. Cutkosky, Robotics and Automation, 2007 IEEE International Conference on, 2007, pp. 1268–1273.
18 L. F. Boesel, C. Greiner, E. Arzt and A. Del Campo, *Adv. Mater.*, 2010, **22**, 2125–2137.
19 J. Lee and R. S. Fearing, *Langmuir*, 2008, **24**, 10587–10591.
20 C.-Y. Hui, A. Jagota, L. Shen, A. Rajan, N. Glassmaker and T. Tang, *J. Adhes. Sci. Technol.*, 2007, **21**, 1259–1280.
21 S. Chary, J. Tamelier and K. Turner, *Smart Mater. Struct.*, 2013, **22**, 025013.
22 M. D. Bartlett, A. B. Croll, D. R. King, B. M. Paret, D. J. Irschick and A. J. Crosby, *Adv. Mater.*, 2012, **24**, 1078–1083.
23 D. R. King, M. D. Bartlett, C. A. Gilman, D. J. Irschick and A. J. Crosby, *Adv. Mater.*, 2014, **26**, 4345–4351.
24 M. D. Bartlett, A. B. Croll and A. J. Crosby, *Adv. Funct. Mater.*, 2012, **22**, 4985–4992.
25 M. D. Bartlett and A. J. Crosby, *Adv. Mater.*, 2014, **26**, 3405–3409.
26 K. Kendall, *Proc. R. Soc. London, Ser. A*, 1975, 409–428.
27 A. Kinloch, C. Lau and J. Williams, *Int. J. Fract.*, 1994, **66**, 45–70.
28 S. Xia, L. Ponson, G. Ravichandran and K. Bhattacharya, *J. Mech. Phys. Solids*, 2013, **61**, 838–851.
29 N. S. Pesika, Y. Tian, B. Zhao, K. Rosenberg, H. Zeng, P. McGuiggan, K. Autumn and J. N. Israelachvili, *J. Adhes.*, 2007, **83**, 383–401.
30 A. Ghatak, L. Mahadevan, J. Y. Chung, M. K. Chaudhury and V. Shenoy, *Proc. R. Soc. London, Ser. A*, 2004, 2725–2735.
31 A. Ghatak and M. K. Chaudhury, *Langmuir*, 2003, **19**, 2621–2631.
32 V. Tvergaard, *Adv. Appl. Mech.*, 1989, **27**, 83–151.
33 M. Ashby, F. Blunt and M. Bannister, *Acta Metall.*, 1989, **37**, 1847–1857.
34 A. Molinari and G. Ravichandran, *J. Adhes.*, 2008, **84**, 961–995.
35 K. R. Shull, C. M. Flanigan and A. J. Crosby, *Phys. Rev. Lett.*, 2000, **84**, 3057.
36 J. S. Biggins, B. Saintyves, Z. Wei, E. Bouchaud and L. Mahadevan, *Proc. Natl. Acad. Sci. U. S. A.*, 2013, **110**, 12545–12548.
37 S. Lin, T. Cohen, T. Zhang, H. Yuk, R. Abeyaratne and X. Zhao, *Soft Matter*, 2016, **12**, 8899–8906.
38 U. Seifert, *Phys. Rev. Lett.*, 2000, **84**, 2750.
39 D. Vella and L. Mahadevan, *Langmuir*, 2006, **22**, 163–168.
40 D. L. Henann and K. Bertoldi, *Soft Matter*, 2014, **10**, 709–717.
41 D. Kaelble, *Trans. Soc. Rheol.*, 1971, **15**, 275–296.
42 R. Rivlin, *Paint Technol.*, 1944, **9**, 215–216.